



Mechanical characteristics and microstructural investigation of CMT deposited bimetallic SS316LSi-IN625 thin wall for WAAM

Amit Motwani¹ · Anand Kumar¹ · Yogesh Puri¹ · Nitin Kumar Laure¹

Received: 21 August 2022 / Accepted: 21 October 2022 / Published online: 3 November 2022
© International Institute of Welding 2022

Abstract

Wire arc additive manufacturing (WAAM) has become increasingly popular over the past few years because of its higher deposition rates that allow fabrication of large, near-net-shaped components and associated reduction of machining time and cost. This work investigates the microstructure and mechanical behavior of a bimetallic thin wall structure composed of 316LSi stainless steel and Ni-base alloy 625 fabricated by the cold metal transfer (CMT) process. Microstructure analysis of the bimetallic wall cross section at different locations revealed a columnar solidification structure with epitaxial grain growth between layers. Microsegregation of Nb and Mo was observed in the interdendritic regions of the alloy 625 deposits leading to the formation of NbC and Laves phase. Microhardness traverses across the bimetallic interface revealed a hardness of 160 to 190 HV in the 316LSi while that of the alloy 625 deposit ranged from 220 to 245 HV with no abnormal hardness at the bimetallic interface. Tensile testing was conducted within the 316LSi and alloy 625 build layers and also transverse to the bimetallic interface. Tensile testing conducted across the bimetallic interface resulted in failure in the 316LSi deposit with an average ultimate tensile strength of 660 MPa, yield strength of 412 MPa, and 49.3% elongation. Fractographic analysis revealed ductile rupture in all cases. This study demonstrates that high-quality bimetallic thin wall deposits between an austenitic stainless steel and a Ni-base alloy can be successfully produced by CMT-WAAM.

Keywords CMT · Bimetallic · FGM · SS316LSi · IN625 · WAAM

1 Introduction

Metal Additive manufacturing is currently a topic of high interest in using metallic layers fused together to form a complete structure. Metal AM has the capability of near-net shape manufacturing along with tailored microstructures and composition [1]. Despite the high precision dimensional tolerance of the laser-based AM processes, fabricating bulk layers for large size components is limited. The need for economical techniques compared to powder-fed laser-directed energy deposition (DED) can be accomplished by using WAAM. Wire arc additive manufacturing (WAAM) is the process by which metallic

wire is melted with the help of an arc as a heat source, so exploring the typical arc welding process for layer by layer deposition to contribute in this area [2]. WAAM processes include gas tungsten arc welding (GTAW), gas metal arc welding (GMAW), and plasma arc welding (PAW) [3]. This DED technique of WAAM, due to readily available wire feedstocks, has a higher deposition rate (1 to 8 kg/h) and favors the printing of medium to large near-net shaped components [4–6]. Even if it is restricted in achieving products with high accuracy, surface finish, and low distortion, its capability for a high deposition rate cannot be ignored [7]. Manufacturing of near-net shape components lowers the machining requirements, decreases lead time, and saves the cost of expensive super alloys used in high-end applications such as aerospace, nuclear, marine, power, oil, and gas industries [8–10]. Irrespective of the power source and feeding stock, the DED process generates strong microstructural anisotropy along with residual stresses and distortion [11–13]. WAAM has a significant challenge of high periodic heat input results in large melt pool size affecting grains size and distortion

Recommended for publication by Commission I - Additive Manufacturing, Surfacing, and Thermal Cutting

✉ Amit Motwani
amitmotwani1392@gmail.com

¹ Visvesvaraya National Institute of Technology, Nagpur, India 440010

and hence influencing the geometrical features. Reduction of heat input is a significant factor in the application of WAAM technology. Cold metal transfer (CMT) is the recent advancement in the gas metal arc welding (GMAW) technology developed and patented by Fronius, Austria. It uses the upgraded form of short-circuiting mode with a synergic controlled dip transfer mechanism meeting the lower heat input along with other advantages of low spatter and stable arc [14, 15]. These features of CMT favor its utilization in the area of WAAM.

The need for specific properties at specific locations has also led to the attraction towards functionally graded material (FGM) and hence to lower the cost of manufacturing the whole component with single expensive material. FGM offers versatility in component design since it can simultaneously achieve varied material qualities at different regions of a single component [16]. Several attempts and performance analyses [17]–[24] are being made to manufacture metallic FGM with the help of metal AM techniques. Metallic FGM can be classified into three types such as continuous varying, step-wise (discrete) varying, and bimetallics with/without interlayers [17, 18]. Investigations on manufacturing FGM with laser-based DED processes such as laser powder bed feeding (L-PBF), laser engineered net shaping (LENS), and laser-directed metal deposition (LDMD) have been performed with various combinations of alloys. Tailoring of composition gradients is done by controlling the powder feed rates of different alloys into the molten pool [19, 20]. Xinchang Zhang et al. deposited SS316L and IN625 using powder-fed DED with and without an interlayer between the alloys. The effects of interlayer made with a mixture of the same powder materials were investigated, where gradual changes in microstructure and microhardness were observed [21]. Onuike et al. found that a bimetallic build of IN718-Ti64 showed cracking and delamination with both direct deposition and gradient composition. To overcome this, an intermediate bonding layer made by an optimized mixture (3:3:4) of IN718, Ti64, and VC was used [22]. Kim et al. demonstrated a FGM by LENS with selective discrete composition in steps of 10% from IN718 to SS316 and reported segregates in interdendritic regions. Defects such as critical pores and cracks were observed in the range of 20–30% IN718 due to ceramic oxides, intermetallic, and carbide formations [23]. In another study, a similar thin wall of SS316L/IN625 with 10% steps from pure SS316L to IN625 was fabricated by Chen et al. They observed several large and irregular white secondary phases referred as Laves phase along the boundaries of dendrites when the composition of IN625 exceeded 80% [24].

While numerous investigations on dissimilar metal joining and FGM by using powder-fed DED have been performed, little has been explored for wire feeding DED.

Attempts have been made to fabricate varying composition alloys by using a plasma multiwire process [25, 26] and dual wire feeding with GTAW [27]–[29] and GMAW [30]. Abe et al. investigated mechanical properties of equivalent to SS304 and IN600 dissimilar metal deposition by GMAW, suggesting that wire-based DED is more suitable for dissimilar metal deposition than laser and powder DED. They also presented path planning for the fabrication of functional structures by using two welding torches for switching material with the help of a controller [31]. In another study, the evaluation of fatigue strength for SS904L and Hastelloy C276 bimetallic deposition by GMAW was performed by Kannan et al. [32]. The effects due to repeated cyclic higher heat input and heat accumulation with these metal additive manufacturing techniques can be reduced by using the CMT mode for GMAW. Ahsan et al. examined a CMT deposited dual metallic stacked wall of low carbon steel and SS316L. Various heat treatment conditions were analyzed to observe the effects on microstructural and mechanical properties. They concluded that heat treatment above 950 °C did not significantly improve the strength and ductility [33]. Senthil et al. investigated the IN825-SS316L bimetallic fabricated by WAAM-CMT and showed microstructure transition at the interface region from elongated dendrites to fine equiaxed dendrites. Laves phase was also identified at the tensile fracture surface [34].

The bimetallic combination used in the present work consists of Inconel 625 and Stainless Steel 316LSi due to their varied field of applications. Some studies have already been conducted with this combination, including a CMT multitrack deposited bimetallic block [35] and a GMAW deposited bimetallic wall where dwell time between layers was kept fixed at 120 s [36]. SS316L is a low carbon austenitic steel possessing outstanding toughness widely used in applications such as exhaust manifolds, cryogenic processes, petrochemical, paper, and food industries. IN625 is a nickel-based alloy with properties for maintaining its strength even at higher temperatures and strong resistance to corrosion and fatigue stress. So, it is used explicitly in parts of jet engines, seawater equipment, turbine blades, and power, chemical, oil, and gas extraction sectors. The need for research in manufacturing metallic multimaterial and functionally gradient material by WAAM is currently a topic of interest. However, the critical difficulty of high heat input with multilayer deposition still exists, which can be significantly lowered by using the CMT variant. Here, the objective of the study is depositing a WAAM bimetallic thin wall with an interlayer temperature of 80–100 °C as one of the key differences with respect to the parameters of previously carried studies. The combination is deposited using the CMT variant of GMAW with an in-house developed experimental setup.

Microstructural features and mechanical integrity of the bimetallic SS316LSi-IN625 are also presented.

2 Materials and methods

The substrate used for experimentation is stainless steel 316L plate of 200 mm × 40 mm × 12 mm. Commercial 1.2-mm diameter filler wires of grade ER316LSi and ERNiCrMo-3 were used. The chemical composition of the substrate is confirmed by the optical emission spectroscopy, and that of wires are also being provided by the manufacturer, as shown in Table 1. Sixty layers of deposition, which consists of 30 layers for SS316LSi on the substrate and the rest 30 layers for IN625 continuing on the deposited SS316LSi wall, were performed. The power source used for depositing this dual metallic thin wall in CMT continuous wave mode was of Fronius TPS 400i. Two-way scanning strategy is adapted for layer depositions, as shown schematically in Fig. 1. To achieve this, the CMT welding torch position was kept fixed, and the substrate was provided with the travel speed on a motorized servo control X–Y slide. After the deposition of each layer, the substrate was lowered by 2 mm in the Z direction by using a stainless steel lab jack. The setup for conducting the experiment is shown in Fig. 2, and the process parameters with their values used for the bimetallic deposition are listed in Table 2.

The 105-mm-height and 160-mm-long deposited bimetallic wall with locations of microstructure, microhardness, and

tensile specimens is shown in Fig. 3. The average thickness of the deposited wall was 5.6 mm for SS316LSi and 5.5 mm for IN625. To prepare the surface for microstructure specimens, ground on a series of silicon carbide sheets with grit sizes of 220, 400, 600, 800, 1000, 1200, 1500, and 2000. Subsequently, they were polished with diamond polishing agent of 3- μ m and 1- μ m particles and chemically etched with freshly prepared aqua regia (9 ml HCl:3 ml HNO₃) for the time durations of 5–10 s. The microstructure was evaluated by using an optical microscope (Radical), and microhardness evaluation was conducted by the Mitutoyo microhardness tester (HM-12) at a load of 200 gm with a dwell time of 15 s. According to ASTM E8 standard specifications, tensile specimens from the deposited wall were extracted by using a wire-cut EDM and ground to uniform thickness throughout the specimen. Uniaxial tensile tests were performed at the extension rate of 3 mm/min on Instron 4467 UTM machine with 30 KN load capacity. Detailed microstructure and fracture surface morphologies were observed by a JOEL 6380A SEM equipped with EDX analyzer.

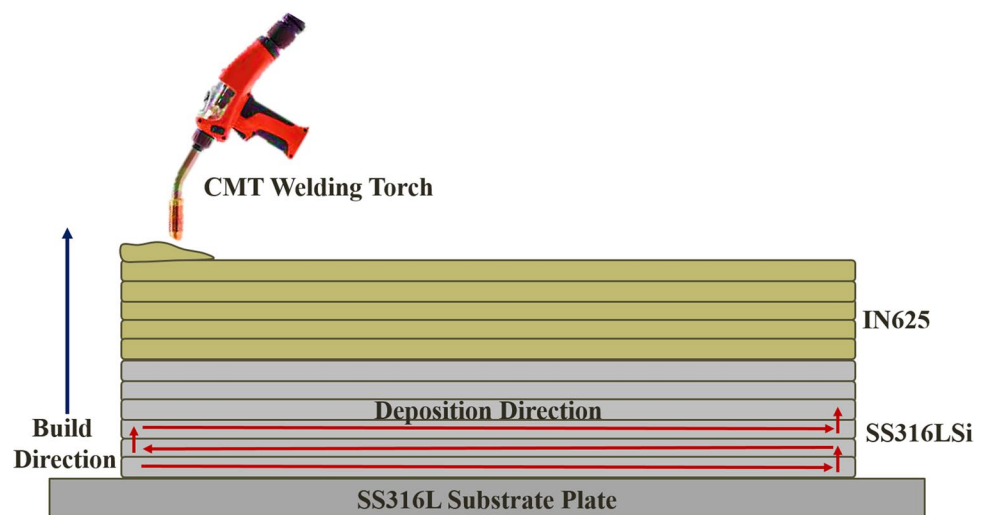
3 Experimental results and discussion

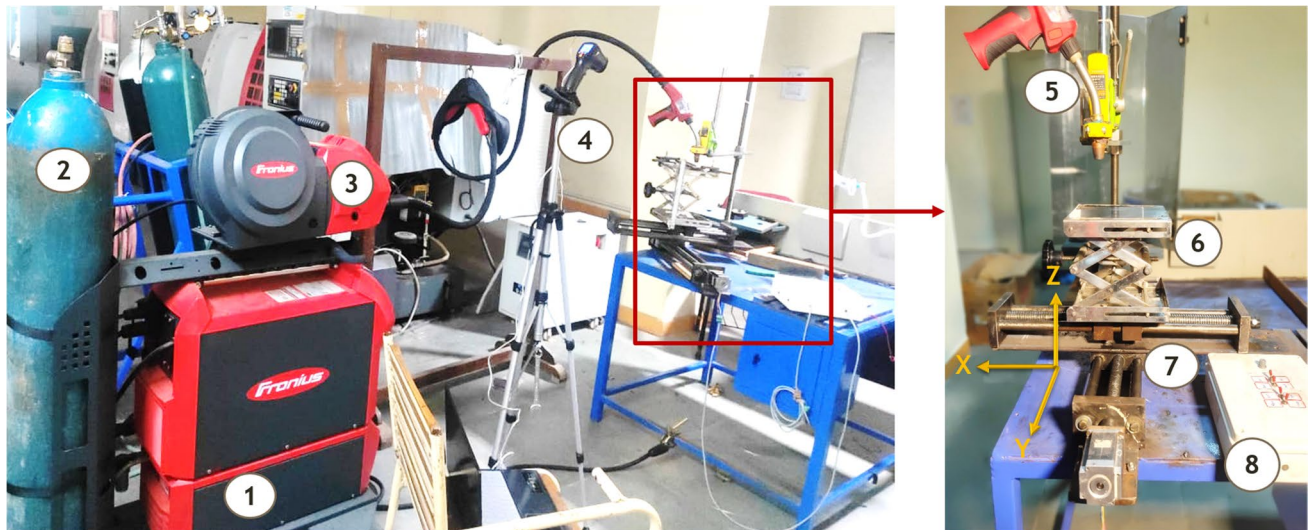
Figure 4 shows the macrostructure and optical microstructure of the interface between SS316LSi and IN625 bimetallic wall revealing a strong metallurgical bond without any visible defects and evidence of solidification cracks. The

Table 1 Chemical composition (wt.%) of substrate plate and filler wires

	Fe	Ni	C	Cr	Mo	Mn	Si	S	P	Cu	Nb+Ta	Al	Ti
Substrate (316L)	Bal	9.974	0.022	16.83	2.134	1.228	0.397	0.001	0.024	-	-	-	-
ER316LSi	64.9	11.88	0.016	18.32	2.537	1.531	0.728	0.010	0.012	0.084	-	-	-
ERNiCrMo-3	1.6	64.51	0.02	20.45	9.4	0.19	0.14	0.004	0.011	0.016	3.546	0.06	0.062

Fig. 1 Bimetallic deposition strategy by CMT-WAAM





1:Welding Power Source 2:Shielding Gas Cylinder 3:Wire Feeder 4:IR Thermometer 5:CMT Torch 6:Lab Jack 7:X-Y Slide 8:Controller

Fig. 2 Experimental setup

Table 2 Process parameters for deposition of CMT-WAAM bimetallic thin wall

Parameter	Unit	SS316LSi	IN625
Current	Ampere	150	120
Voltage	Volt	12.8	12.8
Wire feed	m/min	5.5	4.2
Travel speed	mm/sec	6	6
Gas flow rate	L/min	15	15
Layer step	mm	2	2
Interlayer temperature	°C	80–100	80–100
Shielding gas	-	98%Ar+2%CO ₂	99.99%Ar

bimetallic interface is between the top layer of SS316LSi deposited wall and the first layer of IN625. The presence of dark constituents of δ -ferrite within the γ -austenite matrix can be seen in the SS316LSi. Also, it is visible as fully austenitic on the IN625 side, similarly identified in all Ni-based alloys with solid solution strengthening [37]. Elemental mapping for individual elements across the interface region is presented in Fig. 5. It can be seen that only Cr is evenly distributed on either side of the interface as both the alloys contain almost similar levels of it. While elements such as Ni, Mo, and Nb are rich in the IN625 region, Fe has an obvious higher concentration on the 316LSi region.

The optical micrographs of the SS316LSi layers are presented in Fig. 6, where the fusion boundary is visible in a semi-elliptical morphology. The micrograph of SS316LSi reveals that it consists of columnar dendritic structure. Refined dendritic grains with cellular morphology without any secondary arms are observed at the bottom of the

deposited layer, illustrated just above the fusion boundary. These are grown vertically upwards along the build direction into coarse grains, which can be seen below the fusion boundary. Similar results of the shift in microstructure from cellular to fine columnar to coarse columnar across the SS316L layers were reported by previous examinations [38, 39]. These cellular dendrites with almost no secondary arms are due to the faster cooling rates near the bottom of a layer compared to the top of that layer. Some studies have also been carried out to observe the effects of dwell time and interlayer temperature between the deposition passes. Lee et al. compared CMT deposited SS316L without any dwell time and a dwell time of 1 min between the passes where they reported no prominent changes in the structures [40]. Whereas Yang et al. kept a dwell time of 2 min between the stainless steel GTA deposited layers and showed a significant change in the substructure across the interface [41], it can be noted that fixed dwell time will not lead to a fixed interlayer temperature as the layers and heat accumulation keep on increasing which results in varying cooling rates. Cunningham et al. investigated the effects of heat input and interlayer cooling on the microstructure and mechanical properties of thin-walled 316LSi parts. Interlayer temperatures of 50 °C and 160 °C combined with the low and high heat input were analyzed. The change in substructure across the layer interface with the lower interlayer temperature was more significantly observed compared to the higher interlayer temperature [42]. So, this drastic change of coarser to finer substructure size is attributed to the cooling of the deposited layer almost to the room temperature which enhances the cooling rate of subsequent layer. Figure 6c shows a similar dramatic

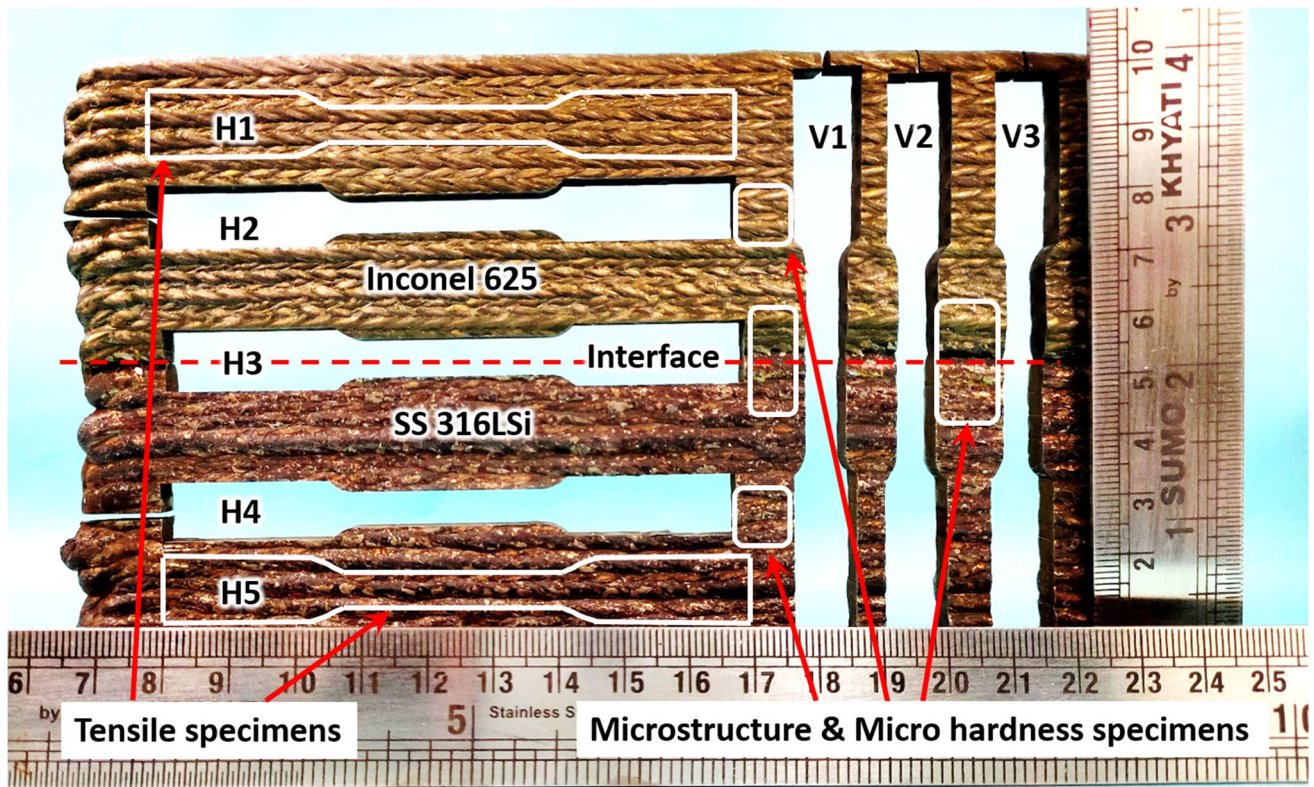


Fig. 3 Deposited bimetallic WAAM wall with locations of extracted specimens

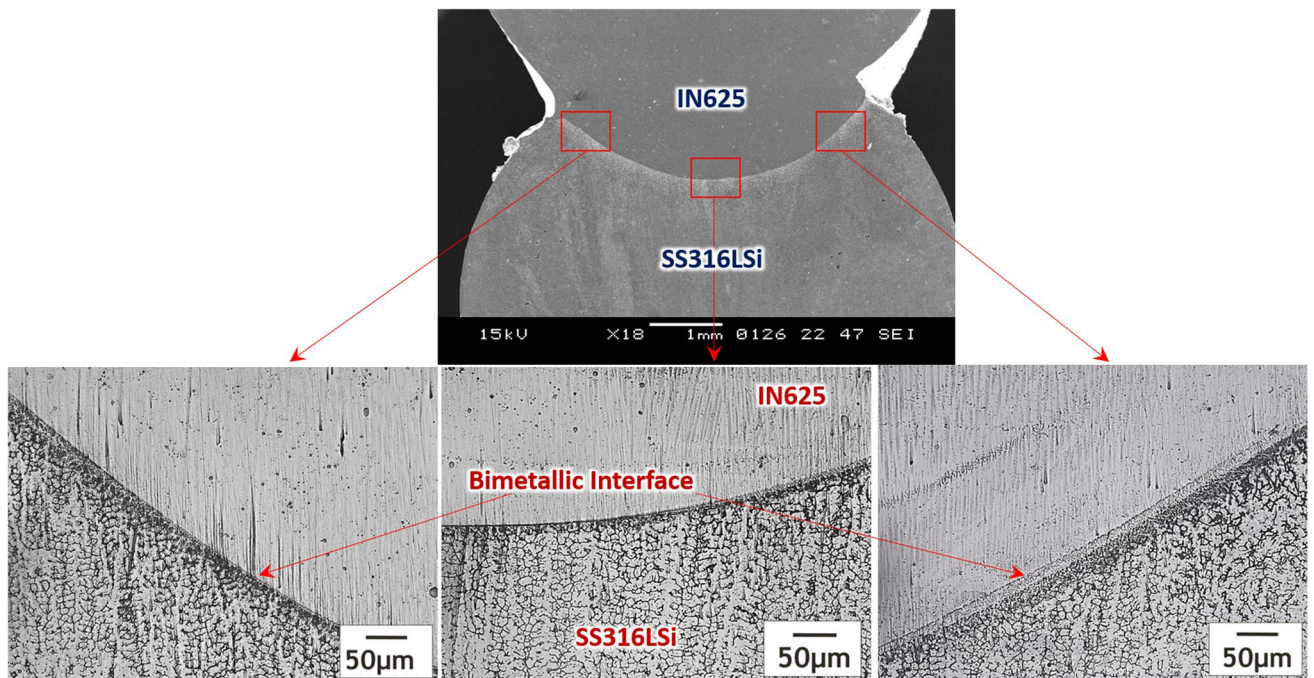


Fig. 4 Optical micrographs of the bimetallic interface

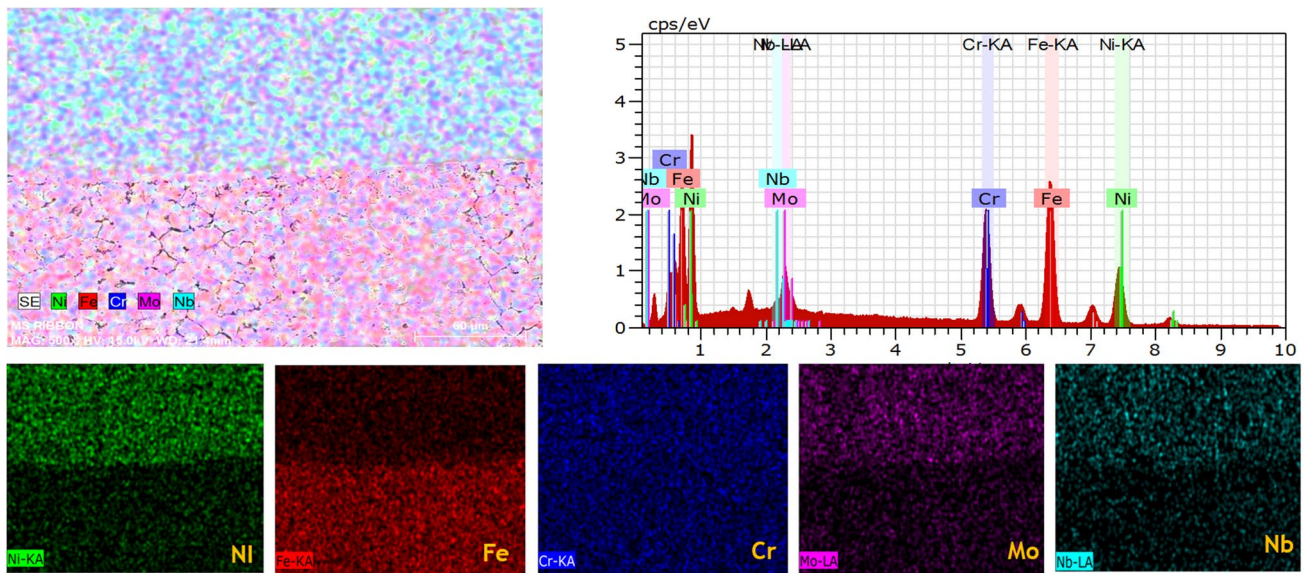
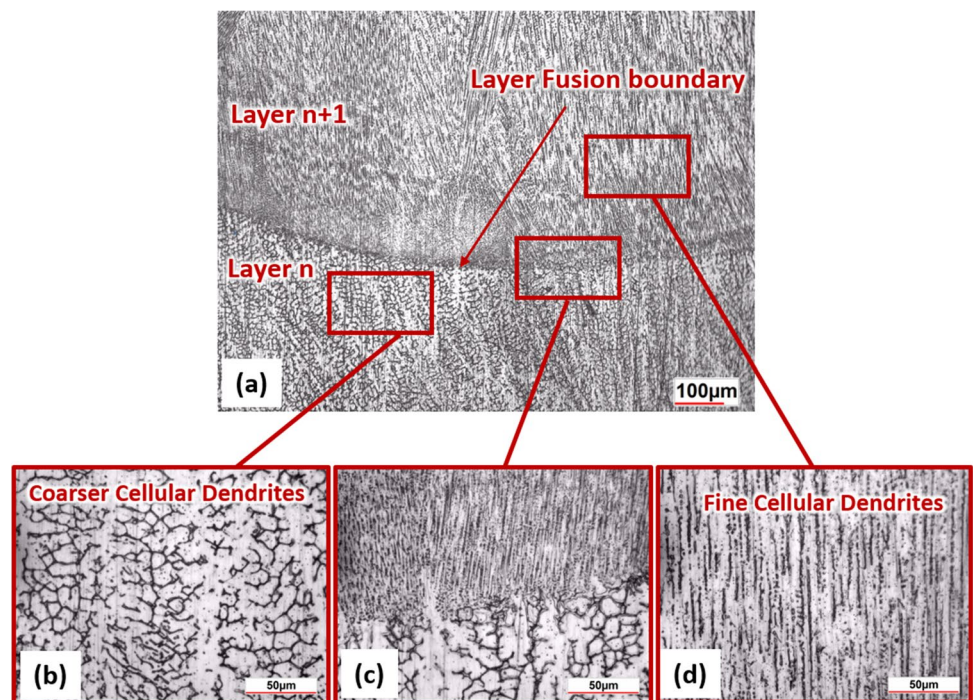


Fig. 5 Elemental mapping at the bimetallic interface

Fig. 6 Optical micrographs of the SS316LSi layers



change of the substructure across the layer interface of SS316LSi as the interlayer temperature of 80–100 °C is used in this investigation. To further quantify the change of substructure across the layer fusion boundary, primary dendrite arm spacing (DAS) is calculated by analyzing the images in ImageJ software. The primary DAS just below the interface is calculated as 11.36 µm while that of the fine structure just above the fusion boundary is found near

to 2.76 µm which describes the change in structure by a factor of around 4.12. While it is observed that primary DAS changed by a factor of around 1.78 when the interlayer temperature of 200 °C was maintained in a previous investigation [43], also it changes by a much lower factor of around 1.47 when lower dwell time (up to 20 s) and uncontrolled interlayer temperature are used [38, 44]. Hence, it is expected to observe the change in substructure

by a greater factor when the interlayer temperature goes on decreasing.

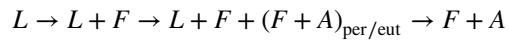
The higher resolution SEM images are examined with spot EDS by obtaining the elemental composition as represented in Fig. 7. It is found that the darker regions are rich in Cr and Mo content as compared to the light in color spaces which consist of higher Ni content. So, it exhibits the dark-colored skeletal ferrite (δ phase) distributed within the light in color matrix of austenite (γ phase). The chromium to nickel equivalent ratio (Cr_{eq}/Ni_{eq}) is calculated by Eqs. 1 and 2 from WRC-1992 diagram to determine the solidification mode and ferrite number (FN) [45, 46]. This Cr_{eq}/Ni_{eq} ratio below 1.2 denotes the austenite mode (A) of solidification, while a ratio between 1.2 and 1.5 yields the austenite-ferrite (AF) mode, and a ratio above 1.5 depicts the ferrite–austenite (FA) mode of solidification.

$$Cr_{eq} = Cr + Mo + 0.7Nb \tag{1}$$

$$Ni_{eq} = Ni + 35C + 20N + 0.25Cu \tag{2}$$

By using the above equations with elemental composition data from Table 1, Cr_{eq} , Ni_{eq} , and Cr_{eq}/Ni_{eq} is evaluated as 20.857, 12.461, and 1.67, respectively. So, it confirms the ferrite–austenite (FA) mode of solidification as Cr_{eq}/Ni_{eq}

obtained is well above 1.5 and has the following solidification sequence [45]:



where L , F , and A denote the liquid, ferrite, and austenite, respectively. The solidification mode determines the formation of primary ferrite and austenite forms at the end of process by a peritectic reaction. Also, the ferrite number (FN) obtained by WRC 1992 diagram is between 7 and 9. The Schaeffler’s diagram is also used to confirm the solidification mode and for predicting the amount of ferrite in austenite matrix [46]. The ferrite percentage obtained by using the Schaeffler’s diagram is around 8%.

The optical micrograph of deposited IN625 above the interface across the cross section of the build direction reveals the microstructures consisting of cellular dendrites, as shown in Fig. 8a and b. The solidification subgrain boundaries are an abundantly observed feature in the WAAM process in which the trend of epitaxial grain growth from one layer across another is clearly visible. An increase in dendrite spacing can be seen from the bottom to the top of the layer due to thermal cycles and differences in cooling rates along the buildup direction [47]. Higher resolution SEM images and elemental analysis by EDS are used for a better understanding of the microstructure, as shown in

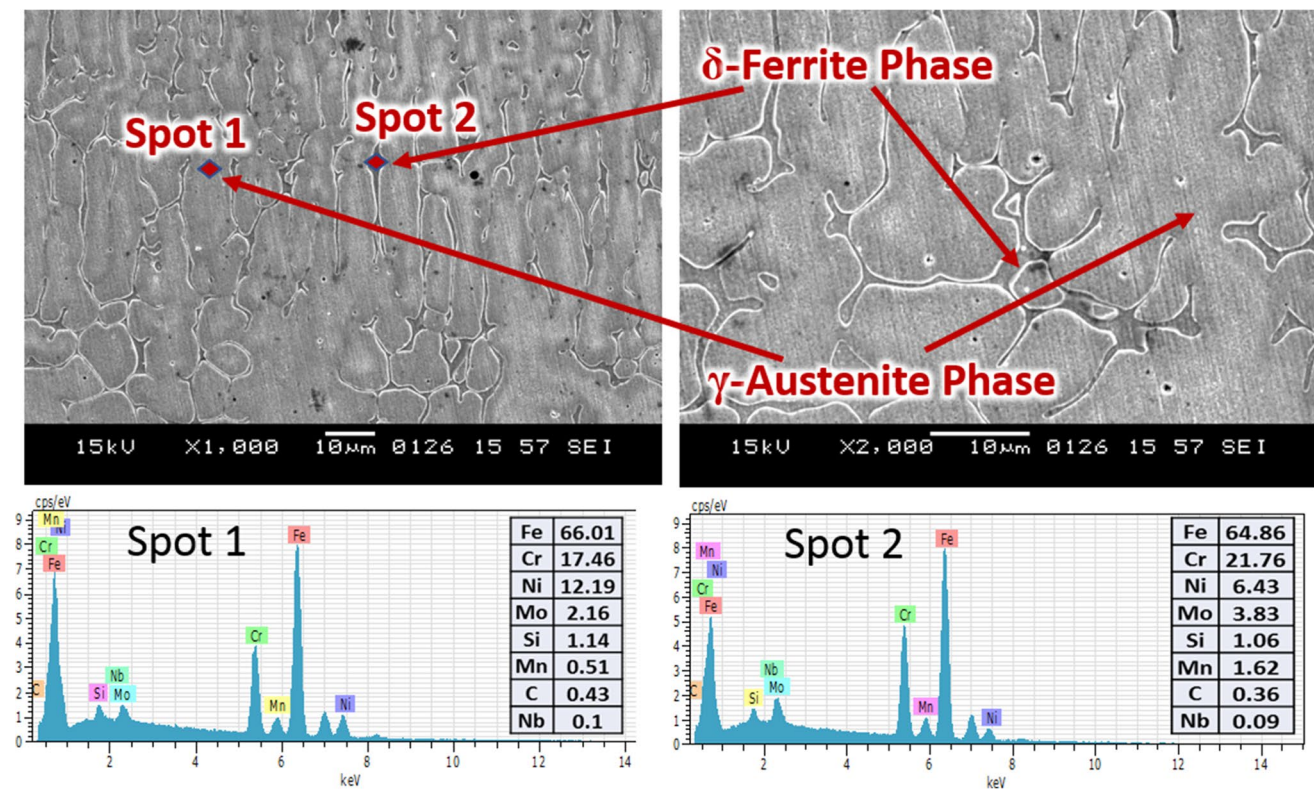


Fig. 7 EDS analysis of SS316LSi microstructure

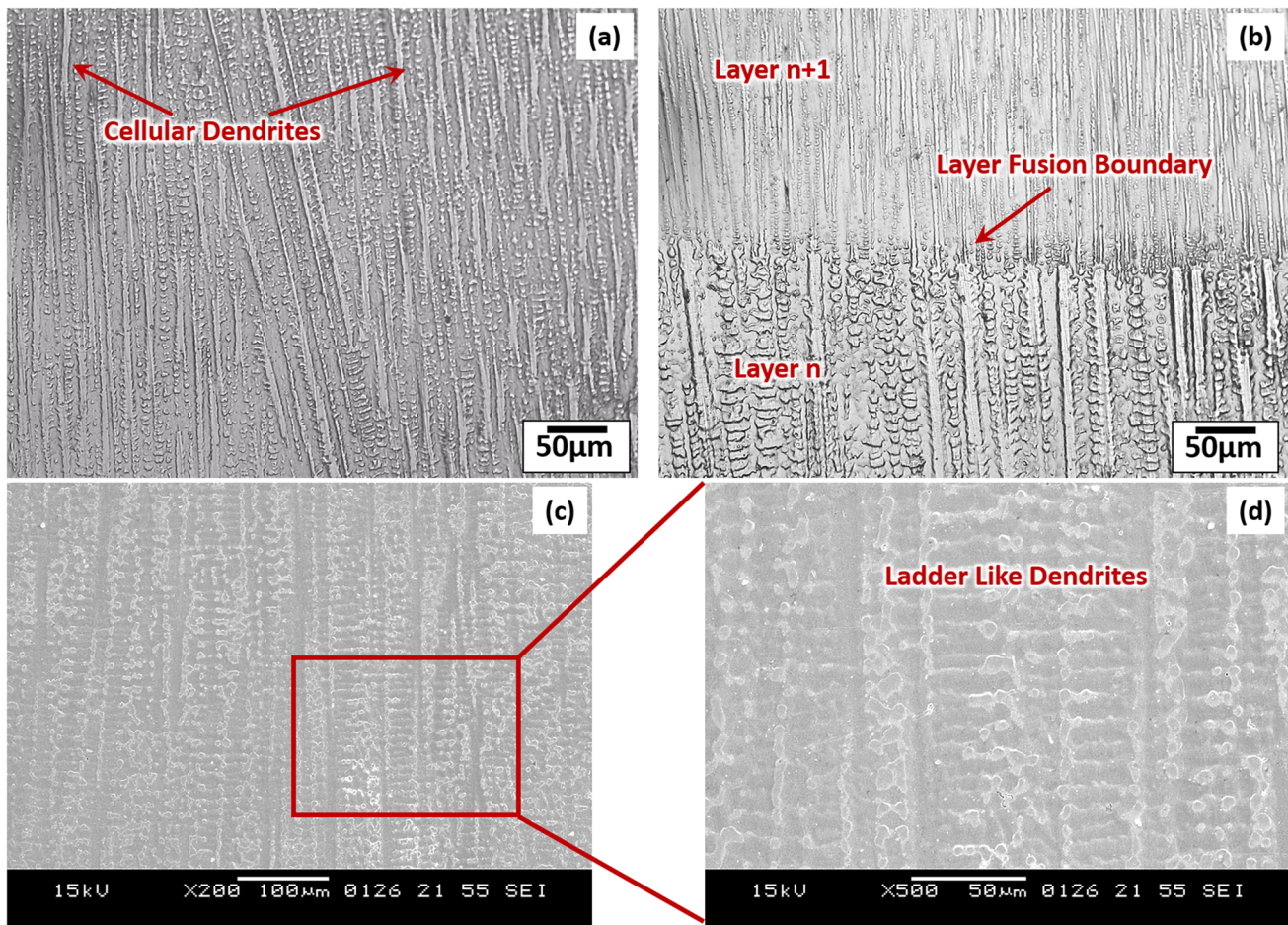
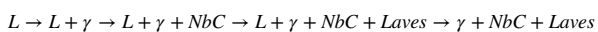


Fig. 8 Micrographs of Inconel 625 layers: **a** and **b** optical images and **c** and **d** SEM images

Fig. 8c and d and Fig. 9 correspondingly. Investigating the elemental map for Ni, Cr, Nb, Mo, and Fe, it is noticeable that the interdendritic spaces are rich in Nb and Mo compared to the dendritic cores. The weight analysis of the spot at interdendritic space confirmed that the elemental composition obtained has comparatively low Ni (~55%) and higher Nb + Mo (~23%) than the dendrite core region with a similar composition to Ni–Cr-based matrix. While Nb is added to IN625 as a solid solution strengthener, a significant amount of it is involved in forming secondary phases in the weld metal. Due to its high tendency to segregate, the subsequent development of the Nb-rich NbC and Laves phases takes place [37]. The general solidification sequence of IN625 is follows as [37]:



When solidification starts, the elements of Nb and C in the liquid phase consume quickly, and eutectic reaction happens, which gradually forms the austenitic NbC eutectic structure. A new eutectic reaction starts when the current eutectic reaction approaches the saturation. The Nb and C

elements continue to consume, and depending on the already developed austenitic matrix, the austenitic and Laves phase eutectic reaction occurs. The Laves phase and NbC are easy to form, but due to the shorter cooling time, the carbide phase of NbC phase formation is restricted, so the NbC phase content is less than Laves phase [48]. While these isolated particles contribute in precipitate strengthening, its continuous presence would only create an embrittling effect. Under high restraint conditions, these can lead to solidification or liquation cracks which were not observed in the deposition of IN625. Laves phases are formed at the last stages of solidification sequence having HCP structure in $(Ni, Cr, Fe)_2(Nb, Ti \text{ and } Mo)$ form [49]. Researches have also reported the existence of second phase particle MC-type carbides [48] and tiny shaped Nb and Ti rich particles [47] in IN625 deposition. The enrichment of Nb with bright irregular regions at grain boundary and interdendritic spaces referred as Laves phase is generally seen in Inconel layers. Laves phase is hard and brittle at room temperature which is undesirable due to its ability to decrease the strength [37]. The obtained higher weight percentage fraction of Nb and

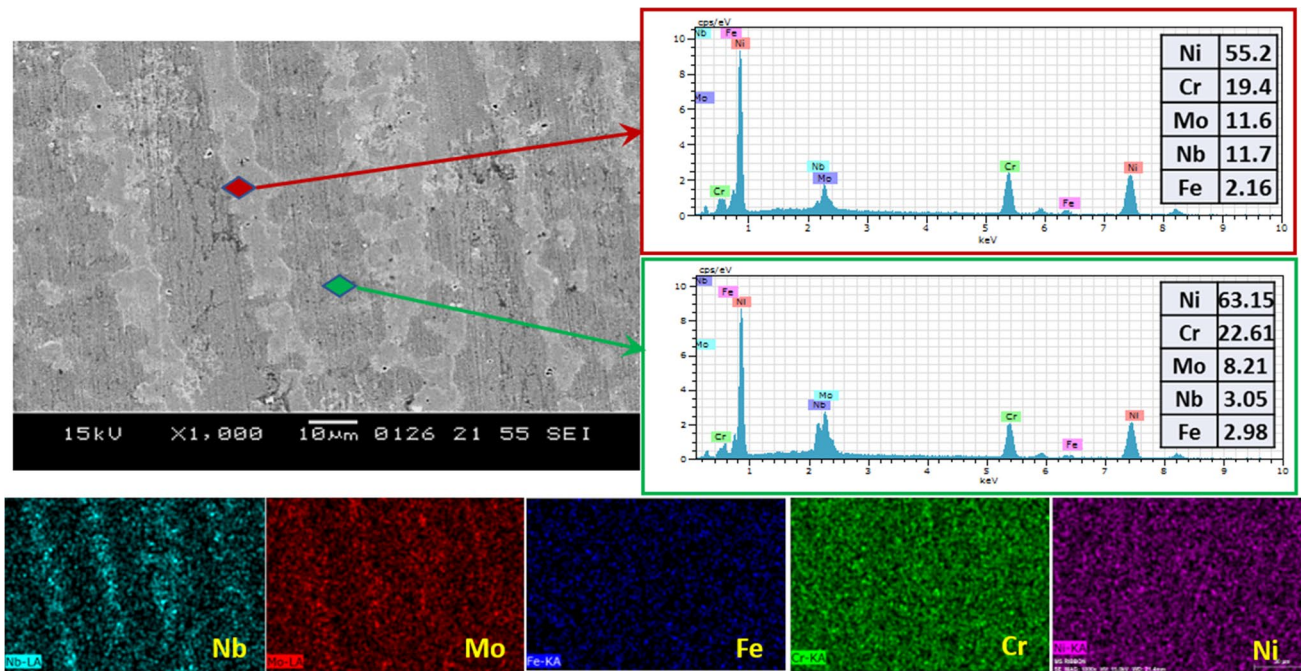


Fig. 9 Elemental mapping of dendrites and its weight analysis at spots for IN625

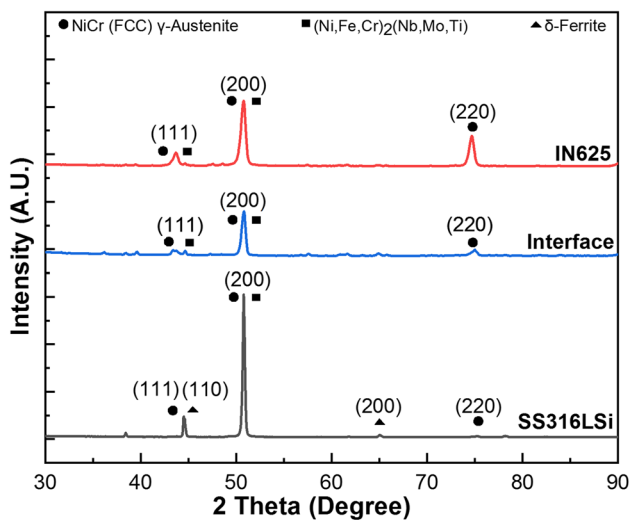


Fig. 10 XRD analysis curve of bimetallic at different regions

Mo in the interdendritic region as shown in Fig. 9 signifies the presence of second phases like Laves phase, and the results are also in agreement with previous work on WAAM of IN625 [48]. So, these secondary phases formation attributes to the segregation of Nb and Mo elements in the non-equilibrium solidification during the deposition process.

To further validate the phases present in the bimetallic deposited wall, XRD analysis was performed at three regions of wall. The XRD data of the regions consisting of SS316LSi, bimetallic interface, and IN625 are shown

in Fig. 10. It is observed that both materials have their major peaks at $2\theta = 50\text{--}52^\circ$ as FCC γ phase. The main grain growth direction is (200), (220), and (111) indicating towards epitaxial grain growth pattern. So, the data represents the phases of Ni-base austenite phase (γ phase) and $(\text{Ni, Cr, Fe})_2(\text{Nb, Mo, Ti})$ as secondary phase in the IN625 region as well as the interface zone, while SS316LSi also consists of γ -austenite phase along with the peaks of δ -ferrite. In this study, the measured $\text{Cr}_{\text{eq}}/\text{Ni}_{\text{eq}}$ ratio is greater than 1.5; therefore, a ferritic-austenitic microstructure is achieved by SS316LSi layers which is being confirmed by the X-ray diffraction.

The microhardness variation at the bimetallic interface and nearby layers is presented in Fig. 11. The hardness of SS316LSi is found in the range of 160–190 HV, while that of IN625 is 220–245 HV. The scattering in hardness value can be because of the reasons that the indents are occasionally made on or near the layers interface, and randomly chosen test position may indent on the secondary phase or the matrix, causing variation in the hardness for the adjacent two positions. It is also observed that the hardness value is a little higher at the bottom and top of the layer, i.e., near the layer’s interface region, attributed to the refined microstructure. The hardness value just before the bimetallic interface is found slightly lower but is in the range of respective alloy materials. Similar observations for a reduction in hardness near the interface with deposition of nickel alloy on stainless steel were also found in the previous investigations of WAAM [31, 50]. Carrol et al. [51] and Chen et al. [24] also reported

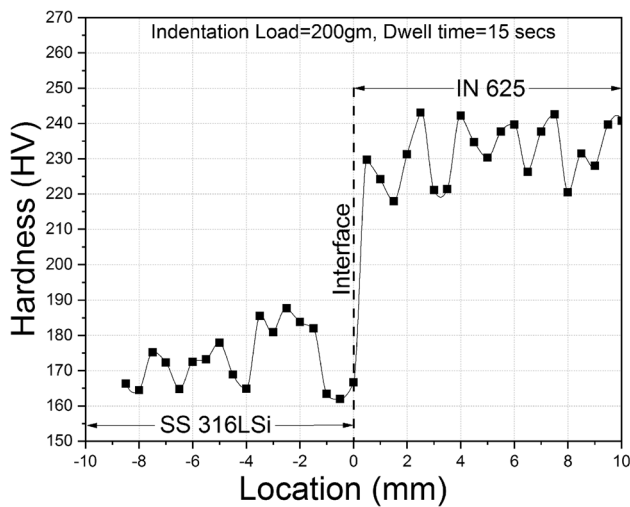


Fig. 11 Hardness variation at SS316LSi-IN625 interface

a decrease in hardness upon introduction of IN625 on stainless steel for manufacturing the FGM by laser DED. The decrease in hardness near the interface zone was because of the FA solidification mode. Upon cooling, the primary ferrite in the microstructure underwent a phase transformation to austenite with a small amount of residual skeletal ferrite [24, 50, 51].

The mechanical characteristics of the bimetallic wall were also analyzed by performing tensile test at the room temperature. The ultimate tensile strength (UTS), yield strength (YS), and elongation percentage of all the individual samples along with the average values are listed in Table 3. The engineering stress vs strain curves of each category closest to the average value are plotted in Fig. 12. Fracture surface observation showed that all the specimens had a typical ductile type of failure. It is observed that all the vertical bimetallic samples fractured on the SS316LSi side confirm a good metallurgical bimetallic bond without any defects. Similar results were also reported by other bimetallic combinations

failing on the weaker side [52, 53]. For vertical bimetallic specimens, average UTS of 660 MPa, YS of 412 MPa, and elongation of 49.3% are obtained. Even though the failure location of the vertical bimetallic sample is on SS316LSi side, its UTS and YS obtained are superior to the previous work on 316LSi deposited wall [42]. Also, the stress–strain curve of the horizontal specimens with bimetallic interface is found identical to the curve of horizontal pure SS316LSi specimens. UTS and YS of the bimetallic horizontal specimen are measured as 507 MPa and 329 MPa, respectively, which is very close to that of the SS316LSi. Horizontal samples have greater elongation than the vertical samples which are also in agreement found in most of the previous studies for WAAM [42, 48, 52]. Elongation percent denotes the measure of ductility, and this severe variation in elongation values shows the anisotropic nature in ductility. The IN625 specimens in the scanning direction had greater elongation percentage as 66.35% compared to the SS316LSi. The average UTS and YS of IN625 was measured as 761 MPa and 415 MPa, respectively, while for the 316LSi, it is found as 502 MPa and 321.5 MPa, respectively. It is found that horizontal specimens have greater UTS and YS compared to vertical ones presented in previous investigation [54]. The reason for this outcome is that horizontal specimen has more grain boundaries, whereas the vertical specimen has more columnar grains. The strength produced by the grain boundaries is greater than the strength produced by the grain itself, resulting in the horizontal tensile specimen being stronger than the vertical one [55].

The SEM images of the fractured specimens are shown in Fig. 13a–f. Higher magnification images depict the presence of dimples features with microvoids in all specimens representing the obvious fracture mode as ductile rupture. The vertical bimetallic samples failed at the stainless steel side, which is confirmed by performing EDS at higher magnification on fractured surface as shown in Fig. 13g indicating a sound bonding of bimetallic interface. The presence of secondary phases initiates as microvoids and can be

Table 3 Tensile testing results of as-deposited bimetallic thin wall (refer Fig. 3)

Sample description	Sample No.	UTS σ_u (MPa)	Avg UTS $\sigma_{u,avg}$ (MPa)	YS σ_y (MPa)	Avg YS $\sigma_{y,avg}$ (MPa)	Elong (%)	Avg Elong (%)
Vertical (IN625-SS316LSi)	V1	662	660	429	412	48	49.3
	V2*	654		402		49.25	
	V3	664		405		50.625	
Horizontal (IN625)	H1*	774	761	425	415	67	66.35
	H2	748		405		65.7	
Horizontal (IN625-SS316LSi)	H3*	507	507	329	329	55.9	55.9
Horizontal (SS316LSi)	H4	499	502	324	321.5	55.6	58.4
	H5*	505		319		61.25	

*Plotted in Fig. 12

Fig. 12 Engineering stress vs strain curves for as-deposited bimetallic specimens in different location with the inset of fractured samples

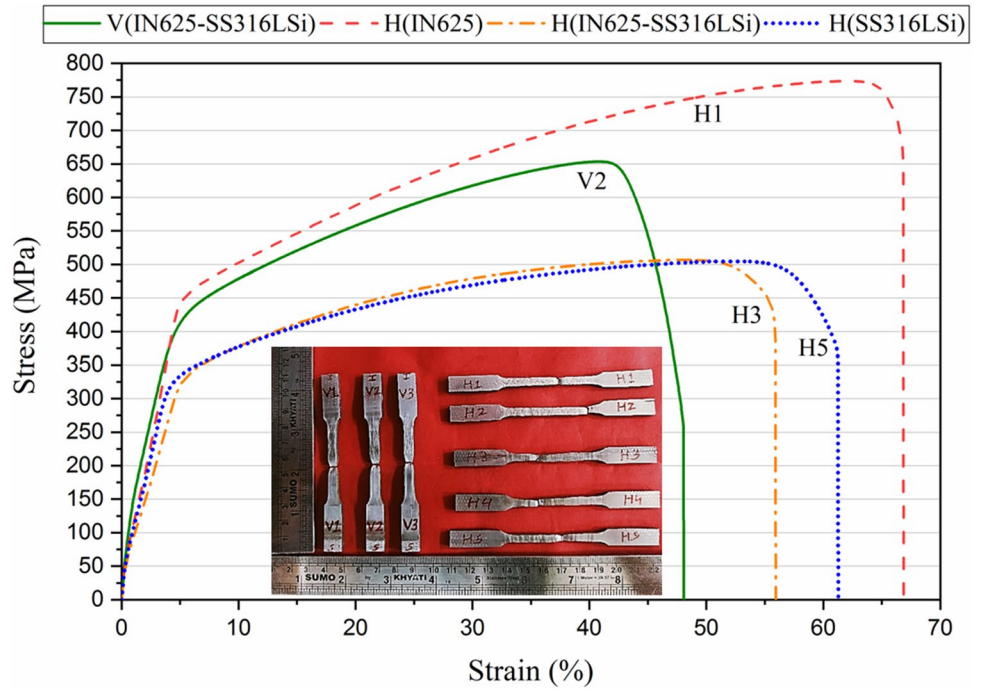
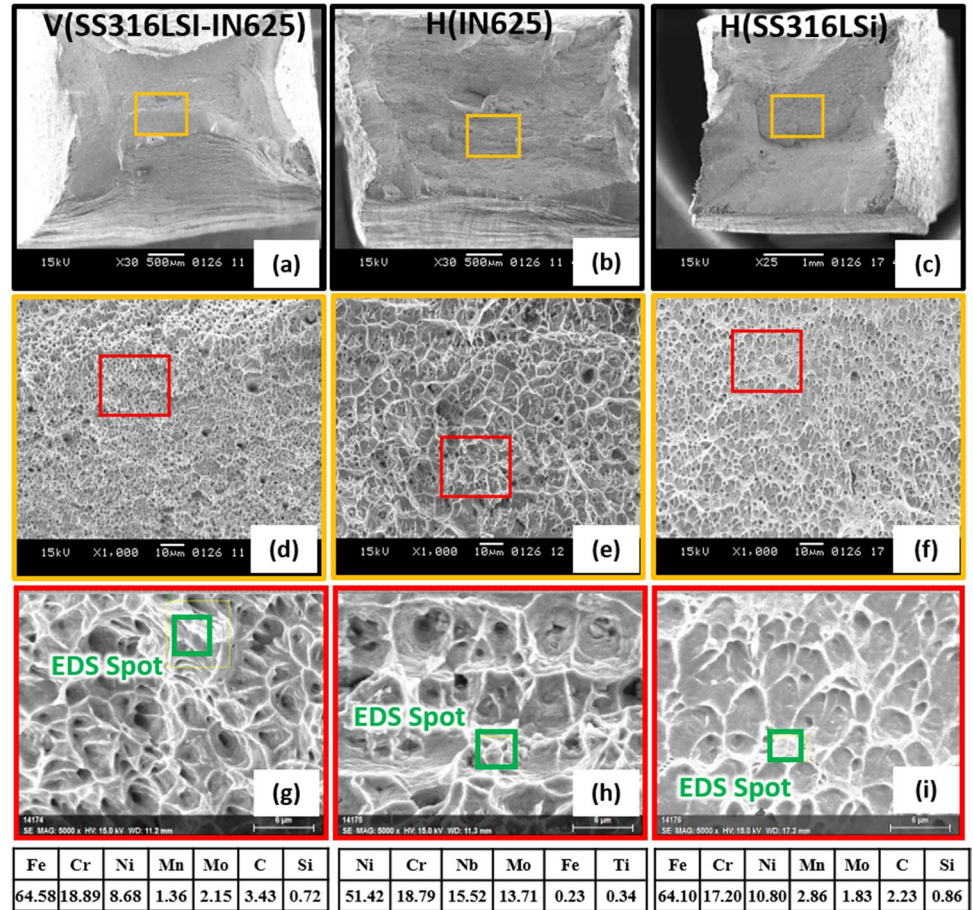


Fig. 13 SEM images of the fractured tensile samples with EDS



responsible for the eventual failure of the SS316LSi samples [39]. The EDS results of IN625 fractured surface presented in Fig. 13h also revealed higher Nb and Mo concentrations than the usual alloy composition, indicating the existence of brittle second phases which is attributed for deteriorating the mechanical properties [56]. A significant portion of the alloying elements used for strengthening the alloy is consumed in precipitate formation. When subjected to plastic deformation, the second phases would weaken the bond at the matrix interface and break into fine particles, forming the condition for crack initiation and propagation [24]. So, this segregation of alloying elements makes the grain coarser resulting in larger dimples on the fractured surface [57] which can be similarly depicted in Fig. 13e.

4 Conclusions

In this investigation, a dual metallic thin wall of SS316LSi and IN625 combination has been successfully deposited by employing the CMT-WAAM. The feasibility of the process is demonstrated to additively fabricate dissimilar alloys with no production defects at the bimetallic interface. The conclusions obtained by this experimental study are as follows:

- Microstructure analysis reveals the epitaxial grain growth in the build direction with non-equilibrium microstructures in deposited layers. The shift of fine cellular dendritic to the coarser structure has been observed along the layer thickness due to the thermal cycles and varying cooling rates.
- SEM analysis of SS316LSi exhibits the skeletal δ -ferrite within the γ -austenitic matrix, while IN625 consists of the γ -austenitic phase with other secondary phases, which were also validated by XRD analysis.
- Segregation of Nb + Mo is detected in the interdendritic regions of IN625 microstructure, indicating the existence of second phases like Laves phase, which was confirmed by conducting the spot EDS.
- Vickers microhardness at the bimetallic interface is observed with the variations being in the range of respective alloys as 160–190 HV for SS316LSi and 220–245 HV for IN625.
- The tensile testing reported sufficient plastic deformation and fracture of the bimetallic specimens in the weaker SS316LSi. UTS and elongation of the bimetallic in the scanning direction are almost identical to that of the SS316LSi. The anisotropy in mechanical properties shows that specimens of scanning direction possess higher elongation and strength than the build direction.
- Fractography observation validates the ductile mode of fracture with the presence of fine dimples. It also revealed the presence of Nb rich brittle second phases in

the IN625 fracture surface resulting in coarser dimples compared to SS316LSi.

Author contribution Manuscript draft, material preparation, experimentation, data collection, and analyses were collectively done by the authors Amit Motwani and Anand Kumar. Facility arrangement, testing support, concept study, and supervision were performed by the authors Yogesh Puri and Nitin Kumar Laatre. All authors read and approved the final manuscript.

Data availability All data generated or analyzed during this study are included in this article.

Code availability Not applicable.

Declarations

Ethics approval Not applicable

Consent to participate Not applicable

Consent for publication Not applicable

Conflict of interest The authors declare no competing interests.

References

1. Duda T, Raghavan LV (2016) 3D metal printing technology. IFAC-Papers Online 49(29):103–110. <https://doi.org/10.1016/j.ifacol.2016.11.111>
2. Chaturvedi M, Scutelnicu E, Rusu CC, Mistodie LR, Mihailescu D, Subbiah AV (2021) Wire arc additive manufacturing : review on recent findings and challenges in industrial applications and materials characterization. *Metals (Basel)* 11(6):939. <https://doi.org/10.3390/met11060939>
3. Martina F, Mehnen J, Williams SW, Colegrove P, Wang F (2012) Technology Investigation of the benefits of plasma deposition for the additive layer manufacture of Ti – 6Al – 4V. *J Mater Process Tech* 212(6):1377–1386. <https://doi.org/10.1016/j.jmatprotec.2012.02.002>
4. Jin W, Zhang C, Jin S, Tian Y, Wellmann D, Liu W (2020) Wire arc additive manufacturing of stainless steels : a review. *Appl Sci* 10(5):1563. <https://doi.org/10.3390/app10051563>
5. Lu X, Zhou YF, Xing XL, Shao LY, Yang QX, Gao SY (2017) Open-source wire and arc additive manufacturing system : formability, microstructures, and mechanical properties. *Int J Adv Manuf Technol* 93:2145–2154. <https://doi.org/10.1007/s00170-017-0636-z>
6. Queguineur A, Rückert G, Cortial F, Hascoët JY (2017) Evaluation of WAAM for large-sized components in naval applications. *Weld World* 62(2):259–266. <https://doi.org/10.1007/s40194-017-0536-8>
7. Jafari D, Vaneker THJ, Gibson I (2021) Wire and arc additive manufacturing : Opportunities and challenges to control the quality and accuracy of manufactured parts. *Mater Des* 202:109471. <https://doi.org/10.1016/j.matdes.2021.109471>
8. Chintala A, Kumar MT, Sathishkumar M, Arivazhagan N, Manikandan M (2021) Technology development for producing Inconel 625 in aerospace application using wire arc additive

- manufacturing process. *J Mater Eng Perform* 16:0–8. <https://doi.org/10.1007/s11665-021-05781-6>
9. Sudhakar R, Sivasubramanian R, Yoganandh J (2017) Effect of automated MIG welding process parameters on ASTM A 106 Grade B pipe weldments used in high-temperature applications. *Mater Manuf Process* 33(7):49–758. <https://doi.org/10.1080/10426914.2017.1401719>
 10. Chandrasekaran S, Hari S, Murugaiyan A (2022) Functionally graded materials for marine risers by additive manufacturing for high-temperature applications: Experimental investigations. *Structures* 35:931–938. <https://doi.org/10.1016/j.istruc.2021.12.004>
 11. Li M, Lu T, Dai J, Jia X, Gu X, Dai T (2019) A Microstructure and mechanical properties of 308L stainless steel fabricated by laminar plasma additive manufacturing. *Mater Sci Eng A* 770:138523. <https://doi.org/10.1016/j.msea.2019.138523>
 12. Le VT, Si D (2020) Microstructural and mechanical characteristics of 308L stainless steel manufactured by gas metal arc welding-based additive manufacturing. *Mater Lett* 271:127791. <https://doi.org/10.1016/j.matlet.2020.127791>
 13. Mukherjee T, Zhang W, Debroy T (2017) An improved prediction of residual stresses and distortion in additive manufacturing. *Comput Mater Sci* 126:360–372. <https://doi.org/10.1016/j.commat.2016.10.003>
 14. Henckell P, Gierth M, Ali Y, Reimann J, Bergmann JP (2020) Reduction of energy input in wire arc additive manufacturing (WAAM) with gas metal arc welding (GMAW). *Materials* 13:2491. <https://doi.org/10.3390/ma13112491>
 15. Selvi S, Vishvakesnan A, Rajasekar E (2018) Cold metal transfer (CMT) technology - an overview. *Def Technol* 14(1):28–44. <https://doi.org/10.1016/j.dt.2017.08.002>
 16. Kieback B, Neubrand A, Riedel H (2003) Processing techniques for functionally graded materials. *Mater Sci Eng A* 362(1–2):81–106. [https://doi.org/10.1016/S0921-5093\(03\)00578-1](https://doi.org/10.1016/S0921-5093(03)00578-1)
 17. Singh DD, Arjula S, Reddy AR (2021) Functionally graded materials manufactured by direct energy deposition : a review. *Mater Today Proc* 47:2450–2456. <https://doi.org/10.1016/j.matpr.2021.04.536>
 18. El IM, Bassiouny G, Mahmoud IS (2019) Functionally graded materials classifications and development trends from industrial point of view. *SN Appl Sci* 1(11):1–23. <https://doi.org/10.1007/s42452-019-1413-4>
 19. Zhang C et al (2019) Additive manufacturing of functionally graded materials : a review. *Mater Sci Eng A* 764:138209. <https://doi.org/10.1016/j.msea.2019.138209>
 20. Debroy T et al (2018) Additive manufacturing of metallic components – process, structure and properties. *Prog Mater Sci* 92:112–224. <https://doi.org/10.1016/j.pmatsci.2017.10.001>
 21. Zhang X, Chen Y, Liou F (2019) Fabrication of SS316L-IN625 functionally graded materials by powder-fed directed energy deposition. *Sci Technol Weld Join* 24(5):504–516. <https://doi.org/10.1080/13621718.2019.1589086>
 22. Onuikwe B, Bandyopadhyay A (2018) Additive manufacturing of Inconel 718 – Ti6Al4V bimetallic structures. *Addit Manuf* 22:844–851. <https://doi.org/10.1016/j.addma.2018.06.025>
 23. Kim SH et al (2021) Selective compositional range exclusion via directed energy deposition to produce a defect-free Inconel 718/SS 316L functionally graded material. *Addit Manuf* 47:102288. <https://doi.org/10.1016/j.addma.2021.102288>
 24. Chen B, Yi S, Zhuohong X, Caiwang T, Jicai F (2020) Development and characterization of 316L/Inconel625 functionally graded material fabricated by laser direct metal deposition. *Opt Laser Technol* 123:105916. <https://doi.org/10.1016/j.optlastec.2019.105916>
 25. Uwe R, Rahul S, Lukas O (2019) Plasma multiwire technology with alternating wire feed for tailor-made material properties in wire and arc additive manufacturing. *Metals* 9:745. <https://doi.org/10.3390/met9070745>
 26. Davis AE et al (2019) Mechanical performance and microstructural characterisation of titanium alloy-alloy composites built by wire-arc additive manufacture. *Mater Sci Eng A* 765:138289. <https://doi.org/10.1016/j.msea.2019.138289>
 27. Chen X et al (2021) A functionally graded material from TC4 to 316L stainless steel fabricated by double-wire + arc additive manufacturing. *Mater Lett*. 300:130141. <https://doi.org/10.1016/j.matlet.2021.130141>
 28. Wu B et al (2020) Enhanced interface strength in steel-nickel bimetallic component fabricated using wire arc additive manufacturing with interweaving deposition strategy. *J Mater Sci Technol* 52:226–234. <https://doi.org/10.1016/j.jmst.2020.04.019>
 29. Rodrigues TA et al (2022) Steel-copper functionally graded material produced by twin-wire and arc additive manufacturing (T-WAAM). *Mater Des* 213:110270. <https://doi.org/10.1016/j.matdes.2021.110270>
 30. Kumar A, Maji K (2021) Microstructure and chemical composition analysis of double wire arc additive manufactured bimetallic structure. *J Mater Eng Perform* 30(July):5413–5425. <https://doi.org/10.1007/s11665-021-05819-9> ASM
 31. Abe T, Sasahara H (2016) Dissimilar metal deposition with a stainless steel and nickel-based alloy using wire and arc-based additive manufacturing. *Precis Eng* 45:387–395. <https://doi.org/10.1016/j.precisioneng.2016.03.016>
 32. Kannan AR, Kumar SM, Kumar NP, Shanmugam NS, Vishnu AS, Palguna Y (2020) Process-microstructural features for tailoring fatigue strength of wire arc additive manufactured functionally graded material of SS904L and Hastelloy C-276. *Mater Lett* 274:127968. <https://doi.org/10.1016/j.matlet.2020.127968>
 33. Ahsan RU et al (2020) Heat-treatment effects on a bimetallic additively-manufactured structure (BAMS) of the low-carbon steel and austenitic-stainless steel. *Addit Manuf* 32:101036. <https://doi.org/10.1016/j.addma.2020.101036>
 34. Senthil TS, Babu SR, Puviyarasan M, Dhinakaran V (2021) Mechanical and microstructural characterization of functionally graded Inconel 825 - SS316L fabricated using wire arc additive manufacturing. *J Mater Res Technol* 15:661–669. <https://doi.org/10.1016/j.jmrt.2021.08.060>
 35. Ahsan MR et al (2021) Microstructures and mechanical behavior of the bimetallic additively-manufactured structure (BAMS) of austenitic stainless steel and Inconel 625. *J Mater Sci Technol* 74:176–188. <https://doi.org/10.1016/j.jmst.2020.10.001>
 36. Sasikumar R et al (2022) Wire arc additive manufacturing of functionally graded material with SS 316L and IN625: Microstructural and mechanical perspectives. *CIRP J Manuf Sci Technol* 38:230–242. <https://doi.org/10.1016/j.cirpj.2022.05.005>
 37. DuPont JN, Lippold JC, Kiser SD (2009) Welding metallurgy and weldability of nickel-base alloys. Wiley. <https://doi.org/10.1002/9780470500262>
 38. Wang C, Liu TG, Zhu P, Lu YH, Shoji T (2020) Study on microstructure and tensile properties of 316L stainless steel fabricated by CMT wire and arc additive manufacturing. *Mater Sci Eng* 796:140006. <https://doi.org/10.1016/j.msea.2020.140006>
 39. Chen X, Li J, Cheng X, He B, Wang H, Huang Z (2017) Microstructure and mechanical properties of the austenitic stainless steel 316L fabricated by gas metal arc additive manufacturing. *Mater Sci Eng A* 703(January):567–577. <https://doi.org/10.1016/j.msea.2017.05.024>
 40. Lee SH (2020) CMT-based wire arc additive manufacturing using 316L stainless steel : effect of heat accumulation on the multi-layer deposits. *Metals (Basel)* 10(278):1–12

41. Yang B, Leu MC (1999) Integration of rapid prototyping and electroforming for tooling application. *CIRP Ann - Manuf Technol* 48(1):119–122. [https://doi.org/10.1016/S0007-8506\(07\)63145-X](https://doi.org/10.1016/S0007-8506(07)63145-X)
42. Cunningham CR, Wang J, Dhokia V, Shrokani A, Newman ST (2019) Characterisation of austenitic 316L stainless steel produced by wire arc additive manufacturing with interlayer cooling. *Solid Free Fabr 2019 Proc 30th Annu Int Solid Free Fabr Symp An Addit Manuf Conf SFF* 426–439
43. Zhong Y, Zheng Z, Li J, Wang C (2021) Fabrication of 316L nuclear nozzles on the main pipeline with large curvature by CMT wire arc additive manufacturing and self-developed slicing algorithm. *Mater Sci Eng A*. 820:141539. <https://doi.org/10.1016/j.msea.2021.141539>
44. Wang C, Zhu P, Wang F, Lu YH, Shoji T (2022) Anisotropy of microstructure and corrosion resistance of 316L stainless steel fabricated by wire and arc additive manufacturing. *Corros Sci* 206:110549. <https://doi.org/10.1016/j.corsci.2022.110549>
45. Lippold JC, Kotecki DJ (2005) *Welding metallurgy and weldability of stainless steels*. John Wiley and Sons
46. Kotecki DJ, Siewert Ta (1992) WRC-1992 constitution diagram for stainless steel weld metals : a modification of the WRC-1988 diagram. *Weld J* 71(5):171–178
47. Tanvir ANM, Ahsan RU, Ji C, Hawkins W, Bates B, Kim DB (2019) Heat treatment effects on Inconel 625 components fabricated by wire + arc additive manufacturing (WAAM)—part 1 microstructural characterization.pdf. *Int J Adv Manuf Technol* 103:3785–3798. <https://doi.org/10.1007/s00170-019-03828-6>
48. Jiang Q et al (2020) Microstructure and mechanical properties of thick-walled Inconel 625 alloy manufactured by wire arc additive manufacture with different torch paths. *Adv Eng Mater* 2000728:1–13. <https://doi.org/10.1002/adem.202000728>
49. Tümer M, Mert T, Karahan T (2021) Investigation of microstructure, mechanical, and corrosion behavior of nickel-based alloy 625 / duplex stainless steel UNS S32205 dissimilar weldments using ERNiCrMo-3 filler metal. *Weld world* 65:171–182. <https://doi.org/10.1007/s40194-020-01011-0>
50. Li T et al (2022) Fabrication and characterization of stainless steel 308 L / Inconel 625 functionally graded material with continuous change in composition by dual-wire arc additive manufacturing. *J Alloys Compd* 915:165398. <https://doi.org/10.1016/j.jallcom.2022.165398>
51. Carroll BE et al (2016) Functionally graded material of 304L stainless steel and inconel 625 fabricated by directed energy deposition: characterization and thermodynamic modeling. *Acta Mater* 108:46–54. <https://doi.org/10.1016/j.actamat.2016.02.019>
52. Kannan AR et al (2020) Microstructure and mechanical properties of wire arc additive manufactured bi-metallic structure. *Sci Technol Weld Join*. <https://doi.org/10.1080/13621718.2020.1833140>
53. Ahsan RU, Newaz A, Tanvir M, Ross T, Elsayy A (2020) Fabrication of bimetallic additively manufactured structure (BAMS) of low carbon steel and 316L austenitic stainless steel with wire arc additive manufacturing. *Rapid Prototyp J* 3:519–530. <https://doi.org/10.1108/RPJ-09-2018-0235>
54. Tanvir ANM et al (2020) Heat treatment effects on Inconel 625 components fabricated by wire + arc additively manufacturing (WAAM) — part 2: mechanical properties. *Int J Adv Manuf Technol* 110:1709–1721. <https://doi.org/10.1007/s00170-020-05980-w>
55. Barba D, Alabort C, Tang YT, Viscasillas MJ, Reed RC, Alabort E (2020) On the size and orientation effect in additive manufactured Ti-6Al-4V. *Mater Des* 186:108235. <https://doi.org/10.1016/j.matdes.2019.108235>
56. Yangfan W, Xizhang C, Chuanchu S (2019) Microstructure and mechanical properties of Inconel 625 fabricated by wire- arc additive manufacturing. *Surf Coat Technol* 374(May):116–123. <https://doi.org/10.1016/j.surfcoat.2019.05.079>
57. Leary M et al (2018) Inconel 625 lattice structures manufactured by selective laser melting (SLM): Mechanical properties, deformation and failure modes. *Mater Des* 157:179–199. <https://doi.org/10.1016/j.matdes.2018.06.010>

Publisher's note Springer Nature remains neutral with regard to jurisdictional claims in published maps and institutional affiliations.

Springer Nature or its licensor (e.g. a society or other partner) holds exclusive rights to this article under a publishing agreement with the author(s) or other rightsholder(s); author self-archiving of the accepted manuscript version of this article is solely governed by the terms of such publishing agreement and applicable law.